40th AIAA/ASME/SAE/ASEE Joint Propulsion Conference and Exhibit
11 - 14 July 2004, Fort Lauderdale, Florida
AIAA 2004-3826
40th AIAA/ASME/SAE/ASEE Joint Propulsion Conference July 12-15, 2004, Fort Lauderdale, FL

Experimental and Numerical Studies of Mixing and Combustion in Scramjet Combustors

S. Menon,* J. Seitzman,† S. Shani,‡ F. Génin,§ T. Thao,¶ K. Miki‖
School of Aerospace Engineering
Georgia Institute of Technology
Atlanta, Georgia 30332
C. Segal,** A. Thakur††
Mechanical and Aerospace Engineering
University of Florida
Gainesville, Florida 32611

1 Abstract

A combined experimental-numerical study is underway to validate a new large-eddy simulation (LES) for supersonic combustion studies. Experimental data on fuel-air mixing is being obtained at Georgia Tech and University of Florida while supersonic combustion is being investigated at University of Florida. The results obtained in the first year's effort are summarized in this paper with particular emphasis on the LES model development and validation.

2 Introduction

Supersonic combustion ramjet (SCRAMJET) is currently being investigated as a propulsion system for several hypersonic applications such as a hypersonic missile, long range passenger transport and Reusable Launch Vehicle (RLV). The successful development of such flying vehicles depends to a large extent, on the development of an efficient propulsion system. Turbojets, which are the most commonly used propulsion systems for subsonic and moderately supersonic aircrafts, lose their advantage of efficiency and economy of operation at Mach numbers above M = 3. Currently, propulsion system of choice for flight in $M = 3$ to 5 regime is a ramjet and beyond that in the $M = 5$ to 15 regimes is the SCRAMJET.

Achieving SCRAMJET propulsion beyond M = 8 is still an unsolved problem since fuel-air mixing, combustion and flame holding in high M stream is a major challenge. Experimental study in ground facilities is also a major challenge and only very limited run-time facilities are available. The most cost-efficient way of investigating the propulsion system performance, therefore, lies in the use of sophisticated computer simulations, provided that the simulation model has the accuracy.

Of particular interest in the numerical development is the ability to predict accurately fuel-air mixing at various operating conditions. Mixing is inherently an unsteady process and requires not only turbulent mixing by the eddies but also molecular diffusion to occur before combustion can take place. Increase in flight Mach number (and hence the Mach number inside the combustor) increases the effective compressibility in the mixing layer. It is well known[1,2] that mixing is inhibited with increase in compressibility. Therefore, the numerical method must be able to predict the effect of compressibility on the mixing process.

Here, we summarize an effort underway under a NASA University Institute program to develop a simulation model to predict fuel-air mixing and combustion in high Mach number flows. Experimental data is being obtained to provide proper inflow conditions to the simulations and also to provide data for model validation. A large-eddy simulation (LES) methodology is being developed for supersonic applications. The computational cost of LES, although significant is fast becoming reasonable with the advent of massively parallel computers.

Although applications of LES to many subsonic non-reacting and reacting flows[3,4,5] have been reported, application to supersonic and/or hypersonic flows has been limited so far. The mixing process that dominates fuel-air mixing at the small scales and the finite-rate kinetics have to be included properly for accurate prediction. This is problematic in classical LES since all the small-scales are modeled, but for accurate prediction of combustion the small-scale features must be resolved. In this paper, we report on the extension of a subgrid scalar mixing model developed earlier for subsonic mixing[6,7,8,9] to supersonic flows.

*AIAA Associate Fellow, Professor
†AIAA Associate Fellow, Assoc. Professor
‡AIAA Member, Research Engineer
§AIAA Student Member, Graduate Research Assistant
¶AIAA Student Member, Graduate Research Assistant
‖AIAA Student Member, Graduate Research Assistant
**AIAA Associate Fellow, Assoc Professor
††AIAA Member, Research Engineer

Copyright © 2004 by Menon et al.. Published by the American Institute of Aeronautics and Astronautics, Inc. with permission.

Copyright © 2004 by Menon et al. Published by the American Institute of Aeronautics and Astronautics, Inc., with permission.

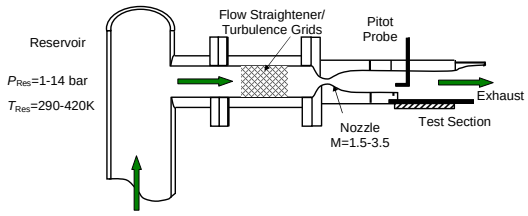

Fig. 1 Georgia Tech supersonic mixing tunnel

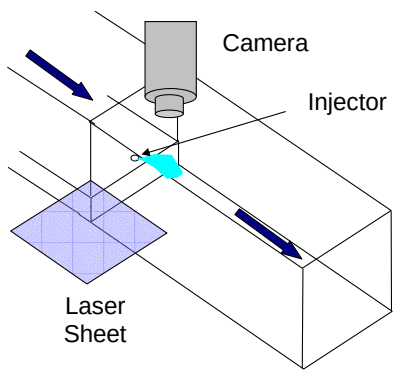

Fig. 2 Schematic of PLIF acetone imaging system

3 Experimental Studies

3.1 Mixing Studies at Georgia Tech

Experiments at GT are being carried out in a M = 2.5 mixing facility (Fig. 1). The wind tunnel can operate at stagnation pressures 0.1-0.4 MPa and stagnation temperature of 290-420 K. Air preheating is accomplished through an indirect, gas-fired heat exchanger. The top and bottom sections of the nozzles are countered while the sides are flat; therefore, the boundary layers are essentially two-dimensional. A rearward facing step (with a step height of 2.46 cm) is used to model a generic scramjet flame holder. The test section has access ports for injection and/or probe insertion. The two sidewalls of the test section are fitted with optical grade, quartz windows (23.5 cm long), allowing for the unobstructed observation of the entire height and length of the test section.

Earlier,[10] stagnation pressure and temperature, static and pitot pressure profiles were measured in both the inlet and downstream of the step using a traversing probe system that can be operated on centerline (Z/h=0) and off-centerline. Wall pressure along the top and bottom walls of the test section were also obtained. All pressures were measured using electrical pressure transducers with an accuracy of 1 percent or better. Static and stagnation temperatures were also obtained at several locations. A sleeved, stagnation temperatures probe is used to measure inlet and downstream stagnation temperature profiles along the centerline of the tunnel. A thermocouple embedded 1mm under the bottom wall of the tunnel, just upstream of the injection location and on the tunnel centerline, measures the inlet wall surface temperature. A second thermocouple is used to measure the external wall temperature of the tunnel (wall thickness = 75mm) at approximately the same axial location.

All the above measurements are typical of what has been obtained in the past in many similar experiments. The current focus however, is on obtain quality data on scalar mixing. Planar laser-induced fluorescence (PLIF) of acetone is being used to measure the fuel distribution and the fuel-air mixing downstream of the injector. For this purpose, acetone is injected just upstream of the center of the step (x/H = -0.24) and normal to the flow. The acetone is injected through a fine atomizing spray injector designed to create a solid cone spray pattern with an 80 degree full angle and a flow rate of 0.95 g/sec. The exit of the injector is flush with the top face of the step. A Phase Doppler Particle Anemometer (PDPA) system is used to characterize the injector performance under quiescent conditions external to the wind tunnel. The measured droplet sizes produced by the injector operating with acetone match a log normal distribution. Droplet velocities are also measured as a function of location, with maximum average velocities of 15-20 m/s.

For the current experiments, the static temperatures in the tunnel are sufficiently low (well below 250 K) such that the acetone will not evaporate, except in the nearly stagnant regions, for example very close to the wall. In addition, the flow velocities are sufficiently high, that freezing of the acetone droplets is not expected to occur within the test section. Thus, the current studies are essentially measurements of a non-evaporating spray. The fluorescence intensity is primarily a function of the acetone volume fraction. Thus, the acetone distribution and the fuel-air mixing in the flow field can be measured.

The acetone PLIF is produce by a pulsed, frequency quadrupled, Nd:YAG laser at 266 nm, with a pulse energy of 100mJ. The laser beam is formed into a thin, collimated, horizontal sheet by a set of three cylindrical lenses. The sheet then passes through the quartz side windows of the test section (Fig. 2). When the ultraviolet laser sheet comes into contact with the acetone, the acetone fluoresces in the visible (400-500 nm) range. An intensified CCD camera viewing from above captures the fluorescence, while a glass camera lens (f/1.8) rejects the ultraviolet laser scattering from the droplets, as well as from the windows of the test section. While the side windows permit the laser sheet to extend upstream of the fuel injector, the top port does not permit the camera to see that far upstream. The laser sheet optics and the camera are mounted on vertical traverses, so that the fuel distribution in any horizontal plane can be determined.

3.2 Mixing Studies at UFA

The facility at University of Florida provides direct connect tests with a variable combustion chamber entrance Mach number of 1.6 - 3.6 and stagnation tem-

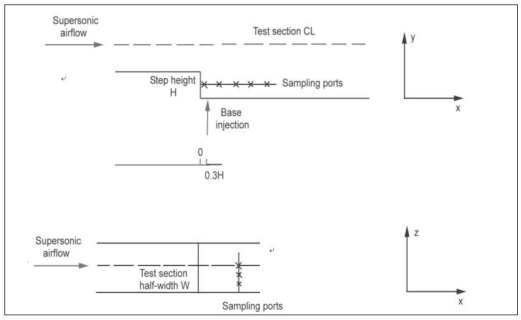

Fig. 3 University of Florida supersonic combustion tunnel

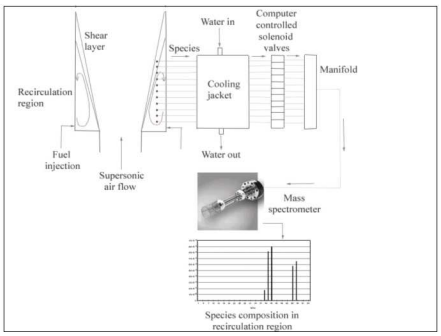

Fig. 4 Mass sampling setup

peratures corresponding to Mach 3.0 - 4.8 flight. All the experiments presented here are performed with combustion chamber entrance Mach 1.6 and cold air. The facility has been described in detail elsewhere.[11] A constant area isolator is placed between the nozzles and the combustor section to protect the nozzle from upstream pressure rise due to combustion in the test section. Optical access is available to the isolator's flow from three sides. The test section is symmetric with ample optical access through covering windows. The isolator cross-section is 2.5 cm x 2.5 cm upstream of the rectangular, rearward facing step having step height H = 1.25 cm, and follows with a constant cross-section area over its 26H length. The test section wall at the base of the step has five fuel injection holes on each side, of 0.5 mm dia equally spaced in a cross section.

So far, cold flow mixing studies at Mach 1.6 using helium as surrogate fuel have been conducted. The inert gas is injected transverse into the air stream at the base of the step. The injection location is shown in Fig 3. The test section window wall covering the step has five mass sampling ports in the recirculation region along the axial x-direction, equally spaced from x/H = 0.2 to 3.2. These ports are 0.6 mm inner diameter steel tubes that end at the test section window wall and do not physically intrude into the recirculation region. In separate tests, other tubes are inserted from the window wall to verify the two-dimensionality of species distribution in the recirculation region. In this case, three stainless steel tubes are placed at x/H = 1.7 and penetrate into the test section to sample species at three different depths, equally spaced in the transverse z-direction from z/W = 0.33 to 1.0. Here W = 1.25 cm is the test section half-width.

A schematic diagram of mass sampling from the recirculation region for subsequent analysis by a mass spectrometer is shown in Fig. 4. The water-cooling jacket shown in the figure is provided to quench the reactions and freeze the species composition coming out of the combustion chamber for the combustion tests that will follow in a future experiment. The sampling ports coming out of the recirculation region are connected to a manifold that has a single outlet going to the mass spectrometer. The input of species to the manifold is regulated by a series of computer-controlled miniature solenoid valves that supply gas mixture from one sampling port at a time for analysis. Sampling from each port is preceded by injection of nitrogen in the manifold to purge the line and flush the species from the previous port, hence preventing mixing of samples from two adjacent ports. The species are analyzed by Stanford Research Systems RGA-300 mass spectrometer that uses electron impact to ionize the gas and a RF quadruple filter to sort species according to their mass-to-charge ratio. The mass spectrometer has an operating pressure range of 10-4 torr (1.3 x 10-7 atm) to ultra high vacuum. It can detect species up to a mass to charge ratio of 300 and has a resolution of 0.5 AMU @ 10 percent peak height.

4 Numerical Studies

For LES, a compressible, second-order accurate, finite-volume LES solver that has been extensively validated and used for many subsonic applications[12,4,9] is employed. This code employs a localized dynamic model equation for subgrid kinetic energy k^{sgs} to close the momentum and energy transport. In this approach, a non-equilibrium model[13] for the sub-grid kinetic energy, k^{sgs} is employed:

$$\frac{\partial \overline{\rho} k^{sgs}}{\partial t} + \frac{\partial}{\partial x_i}\left(\overline{\rho}\tilde{u}_i k^{sgs}\right) = P^{sgs} - \epsilon^{sgs} + \frac{\partial}{\partial x_i}\left(\overline{\rho}\frac{\nu_t}{Pr_t}\frac{\partial k^{sgs}}{\partial x_i}\right) \quad (1)$$

The terms, P^{sgs} and ϵ^{sgs} are respectively, production and dissipation of sub-grid kinetic energy, and are respectively,[14] $\epsilon^{sgs} = C_\epsilon \overline{\rho}(k^{sgs})^{3/2}/\overline{\Delta}$ and $P^{sgs} = -\overline{\rho}\Gamma_{ij}(\partial\tilde{u}_i/\partial x_j)$. Here, $\overline{\Delta}$ is the LES grid scale and the coefficient Pr_t is the turbulent Prandtl number that can be either specified or obtained dynamically. The sub-grid eddy viscosity is $\nu_t = C_\nu\sqrt{k^{sgs}}\Delta$ and the sub-grid stress is modelled as: $\Gamma_{ij} = -2\nu_t(\widetilde{S}_{ij} - \frac{1}{3}\widetilde{S}_{kk}\delta_{ij}) + \frac{2}{3}k^{sgs}\delta_{ij}$, where $\widetilde{S}_{ij}$ is the filtered rate-of-strain tensor, and the coefficients C_ν and C_ϵ are obtained as a part of the solution by using a localized dynamic procedure.[12,3] More details are given elsewhere.[13,3,4]

Scalar mixing using two separate approaches are compared in this study: a conventional gradient diffusion closure at the LES-filtered level and a subgrid

LEM model[15] that incorporates a localized 1-D simulation of the scalar mixing within each LES cell. In conventional LES, the Favre-filtered equation for a scalar Y can be written as:

$$\frac{\partial \bar{\rho}\tilde{Y}}{\partial t} + \frac{\partial}{\partial x_i}[\bar{\rho}\tilde{Y}\tilde{u}_i - \bar{\rho}\tilde{Y}\widetilde{V_i} + Y_i^{sgs} + \theta_i^{sgs}] = 0 \quad (2)$$

Here, $\bar{\rho}$ is the filtered mixture density, and $\tilde{u}_i$ and $\widetilde{V_i}$ are respectively, the $i-th$ component of the filtered flow and diffusion velocities. In this equation, two subgrid terms: $Y_i^{sgs} = \bar{\rho}[\widetilde{u_i Y} - \tilde{u}_i\tilde{Y}]$ and $\theta_i^{sgs} = \bar{\rho}[\widetilde{V_i Y} - \widetilde{V_i}\widetilde{Y}]$ require closure. In the gradient diffusion closure (called LES-GRAD-DIFF, hereafter), θ_i^{sgs} is neglected and Y_i^{sgs} is modeled using an eddy diffusivity closure. Thus, $Y_i^{sgs} = -\frac{\bar{\rho}\nu_t}{Sc_t}\frac{\partial \tilde{Y}}{\partial x_i}$. Here, $Sc_t = 1$ is the turbulent Schmidt Number.

In LES-LEM, molecular diffusion, small- and large-scale turbulent convection, and chemical reaction are all modeled separately but concurrently at their respective time scales. To briefly describe this model split the velocity field as: $u_i = \tilde{u_i} + (u_i')^R + (u_i')^S$. Here, $\tilde{u_i}$ is the LES-resolved velocity field, $(u_i')^R$ is the LES-resolved subgrid fluctuation (obtained from k^{sgs}) and $(u_i')^S$ is the unresolved subgrid fluctuation. Then, consider the *exact* species equation for Y as:

$$\rho\frac{\partial Y}{\partial t} = -\rho[\tilde{u_i} + (u_i')^R + (u_i')^S]\frac{\partial Y}{\partial x_i} - \frac{\partial}{\partial x_m}(\rho Y V_m) \quad (3)$$

In LES-LEM, the above equation is rewritten as:

$$\frac{Y^* - Y^n}{\Delta t_{LES}} = -[\tilde{u_k} + (u_i')^R]\frac{\partial Y^n}{\partial x_i} \quad (4)$$

$$Y^{n+1} - Y^* = \int_t^{t+\Delta t_{LES}} -\frac{1}{\rho}[\rho(u_i')^S\frac{\partial Y^n}{\partial x_i} + \frac{\partial}{\partial x_m}(\rho Y V_m)]dt' \quad (5)$$

Here, Δt_{LES} is the LES time-step. Equation (4) describes the large-scale 3D LES-resolved convection and is implemented via Lagrangian transfer of mass across the finite-volume cell surfaces.[8] Equation (5) describes the subgrid model on the LES space and time scale. The integrand includes all subgrid processes, e.g., subgrid stirring, subgrid molecular diffusion and reaction kinetics that occur within each LES cell. These processes are modeled on a 1D domain embedded inside each LES grid where the integrand is rewritten in terms of the subgrid time and space scales, so that:

$$\rho\frac{\partial Y^k}{\partial t^S} = {F_s}^k - \frac{\partial}{\partial s}(\rho Y^k V^k) \quad (6)$$

Here, superscript k indicates that the subgrid field is further discretized within each LES by N_{LEM} number of subgrid cells along the local coordinate s such that the LES quantity Y is obtained by an ensemble average of the subgrid field. Thus, $Y = \frac{1}{N_{LEM}}\sum_{k=1}^{N_{LEM}} Y^k$. The 1D domain is aligned in the direction of the maximum scalar gradient[15] and the length of the LEM domain is the local LES filter width, $\overline{\Delta}$.

In the above equation, subgrid stirring is symbolically represented as ${F_s}^k$ since it is implemented using stochastic re-arrangement events called *triplet maps*.[15] Each triplet map represents an *instantaneous* action of an isotropic turbulent eddy on the subgrid scalar field. The eddy size l is picked randomly from an eddy size distribution $f(l)$ in the range $\overline{\Delta}$ to η (Kolmogorov scale) and stirring events occur at a specified frequency. Both $f(l)$ and stirring frequency are obtained using inertial-range scaling laws.[15]

The LEM closure is similar to the closure in PDF methods[16] except that molecular diffusion is also included exactly in LES-LEM. As in PDF methods, the large-scale transport is modeled as a Lagrangian transport of the scalar fields across LES cells and the subgrid stirring is modeled. In PDF methods, a mixing model is often employed to model turbulent mixing, whereas in LES-LEM, small-scale turbulent stirring is implemented by the triplet mapping process.

Conservation of mass, momentum and energy at the LES level and conservation of mass, energy and species at the LEM level are strongly coupled.[14,9] Extension to multi-species and finite-rate kinetics have also been demonstrated in the past. Chemical reaction at the LEM level determines heat release and thermal expansion at the LEM level, which at the LES level generates flow motion that, in turns, transports the species field at the LEM level. Full coupling is maintained in the LES-LEM to ensure local mass conservation.

5 Results and Discussion

5.1 Results from Georgia Tech Experiments

Flow visualization (using Schlieren) of the flow past the rearward facing step shows that there is a density boundary layer in the inlet that is around 6 mm thick (0.24H). The initial angle of the expansion from various images ranges from 23-24 degrees above the horizontal, which corresponds (using the Mach angle relationship) to a free stream Mach number of M =2.46-2.56. This is very close to the design Mach number of the nozzle (2.5). The measured shear layer angle is 23-25 degrees. Using this range of flow turn angles (and the range of M), the Mach number after the expansion is estimated to be around 3.83.

Figure 5 presents the inlet pressure and temperature profiles. The static and pitot pressures, normalized to the reservoir pressure, were acquired along the tunnel centerline. Results from off-center (Z/H = 0.284) were found to be similar. The Mach number profile shown in the figure is calculated from the measured static and Pitot pressures. The freestream results (M = 2.59) compares well with the sSchlieren result (M = 2.56). The error bars shown in the figure include both accuracy and precision components. The

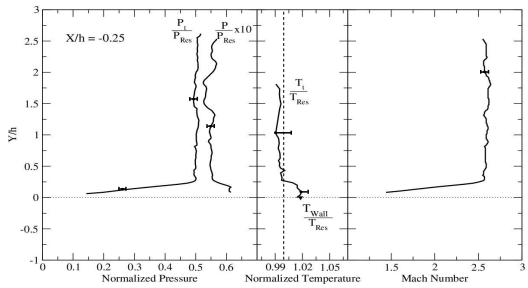

Fig. 5 Inflow profiles for pressure, stagnation temperature and Mach number

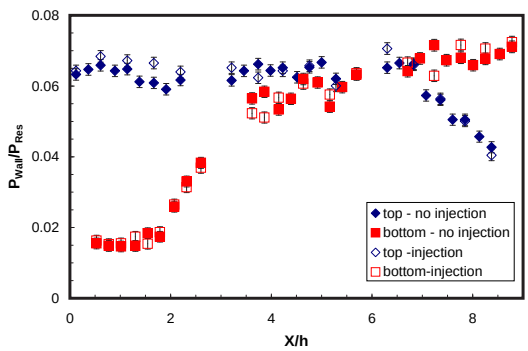

Fig. 6 Wall static pressure profile

pressure and temperature profiles indicate that the bottom wall boundary layer thickness is 0.27h, which compares well the schlieren result (0.24H). From the static pressure profiles, there appear to be some weak waves in the inlet (e.g., from Y/H = 1.25-2.25). These weak waves change the Mach number by only a small amount. As might be expected, the stagnation temperature rises near the wall due to heat transfer from the wall. The normalized bottom wall surface temperature (Twall/Tres) is 1.017, which is quite close to the measured stagnation probe temperature of the flow (1.01-1.02 Tres) just above the wall. Using the inner wall temperature and the external wall temperature measured simultaneously (2-3C above the inner wall temperature), a 1-d heat transfer calculation indicates a heat flux of only 7.3 W/m2 into the flow.

The inflow conditions are used to set proper inflow for the LES studies and is used in a subsequent study. The effect of wall heating appears to be a critical issue as well and is discussed further.

The wall static pressures are shown in Fig. 6. Along the bottom wall the pressure is nearly constant initially, then start to increase at an axial location between X/H = 1.83 and 2.0. This is the location where the shear layer reattaches to the wall and a compression wave is generated. Along the top wall, the pressures are nearly constant until X/H = 7, which would correspond to the upper edge of the expansion fan reaching the top wall. The small variations up to this point are indicative of weak waves in the test section. Figure 6 also shows results for acetone injection. There is little systematic difference between the two results, with and without injection. A similar outcome was seen in the static and stagnation pressure profiles at the inflow and downstream locations.

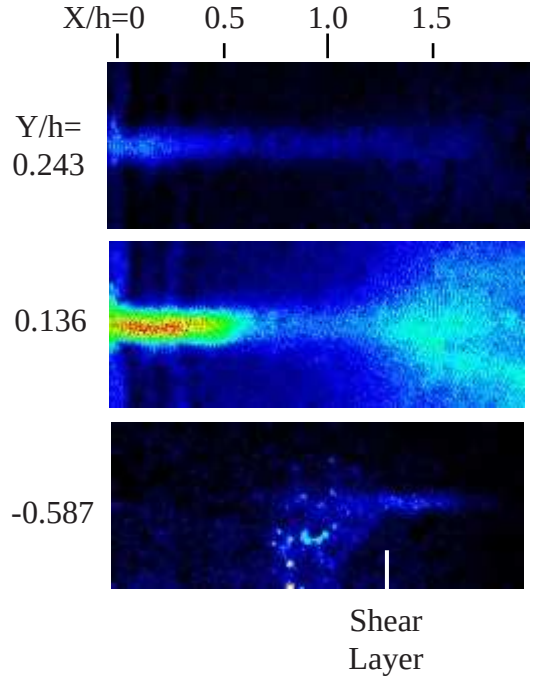

Fig. 7 Preliminary PLIF data

Figure 7 shows some initial results from the acetone PLIF imaging. While the images have been corrected for background, they have not yet been corrected for laser sheet intensity variations. The imaged region extends from just before the step to slightly less than 2H downstream. Average images (based on 10 laser shots each) are shown for three heights in the tunnel. Near the step, the fuel appears to be most concentrated at a height of Y/H = 0.136, with somewhat less concentration at the higher location (Y/H = 0.243). Since the inlet boundary layer extended to 0.24H, it appears that much of the acetone is embedded in the boundary layer, with a small amount of the fuel droplets penetrating into the freestream. Progressing downstream, the acetone concentration appears to continuously decrease for the highest image. For the middle image, the fuel concentration drops suddenly at X/H = 0.65, and then appears to exhibit a sudden lateral spreading at X/H = 1.2 (in the instantaneous images, the acetone appears to split into three distinct pieces). For the lowest image (Y/H = 0.587), there acetone first appears at X/H = 1 or 1.25 (there is a some spurious scattering in this region that makes it difficult to precisely locate the initial acetone location). For comparison, the expected center of the shear layer is indicated, at X/H = 1.3. The loss of signal at the end of the image may be partly due to a reduction in the laser sheet intensity.

Additional measurements are planned in the near future to fully map the mixed fluid distribution in the shear layer. Further LES studies of mixing will be conducted once more detailed data becomes available.

5.2 Results from UFA Experiments

The mass sampling experiments are carried out under steady airflow conditions of $P_{0air} = 4.8$ atm, $T_{0air} = 300$ K and $M_0 = 1.6$ at the isolator entrance. This air stagnation pressure ensures that the flow is supersonic throughout the isolator and the test section. The expansion at the step forms a shear layer and a recirculation region behind the step. Fuel (helium) is injected at steady stagnation pressures and $T_{0fuel} = 300$ K. The stagnation pressures of air and fuel are stabilized to within 0.1 atm of the desired value.

The composition of gas in the recirculation region is analyzed by the mass spectrometer in Partial pressure of species vs. Time mode. The species scanned are nitrogen (m/z = 28, 14), oxygen (m/z = 32, 16) and helium (m/z = 4). Sampling is done sequentially for 10 sec at the purge port and for 15 sec at each of the sampling ports. The local mass fraction of fuel is determined from the partial pressures of nitrogen, oxygen and fuel recorded by the mass spectrometer. The global mass fraction of fuel is determined from the total mass of fuel injected and the total mass of air traveling through the test section.

Mass sampling of the recirculation region species is done in the axial x-direction with helium injected at the base of the step. Helium is injected at two pressures, a moderate stagnation pressure $P_{0He} = 5.4$ atm and a high stagnation pressure $P_{0He} = 12.0$ atm. Each experiment is performed 3 times for repeatability.

The axial distribution of helium mass fraction in the recirculation region for the two helium stagnation pressures is shown in Figs. 8a and b, respectively. Increasing the fuel injection stagnation pressure results in a corresponding increase in the fuel mass fraction in the recirculation region. This indicates that even at high injection pressure much of the fuel remains in the recirculation region and does not have sufficient momentum to escape into the core airflow, which is due to the fact that helium is a light gas. The fuel mass fraction distribution shows more non-uniformity at higher injection stagnation pressure.

The transverse distribution of helium mass fraction at $x/H = 1.7$ in the recirculation region is shown in Figs. 9a and b, respectively for the two helium injection stagnation pressures. At both pressures, the inflow fuel mass fractions are much higher than the wall measured mass fractions, the difference being up to 4-5 times. However, the fuel mass fraction distribution away from the wall is rather uniform, hence indicating a well-mixed fuel-air mixture.

5.3 Numerical Studies and Validation

Since the above experiments are still underway, the LES model has been used in the meantime to study scalar mixing and combustion in other configurations. These results have been reported in detail elsewhere[17,18,19,20] but highlights are included here for completeness. Additionally, some results for the data being obtained at GT and UFA are also discussed here.

5.3.1 Scalar Mixing in Supersonic Shear Layers

LES of scalar mixing in a mixed subsonic-supersonic spatially evolving shear layer have been recently carried out[17,18] and summarized here. This configuration was studied experimentally earlier[21] using a two-stream shear layer made up of air in both streams and PLIF measurements of nitric oxide seeded into the low-speed air is used to obtain scalar mixture fraction data. The two-streams have Mach numbers of 2.0 and 0.4, respectively, which implies a convective Mach number of $M_c = 0.62$. This case is in-between the moderate-to-high compressibility regimes. The supersonic and the subsonic streams enter the test section at a velocity of 480 and 130 m/sec, and at a temperature of 150 K and 252 K, respectively. The stagnation pressures of the supersonic and the subsonic streams are 495 KPa and 75 KPa, respectively. The Reynolds number based on the high-speed momentum thickness at the splitter plate, Re_{θ_1} is 10000 and thus, the shear layer is expected to be turbulent.[21]

A $181 \times 150 \times 5$ grid is used in the streamwise, transverse and spanwise directions, respectively, to resolve a domain that is 50 cm long, 8 cm high and 0.018 cm wide. The shear layer resolution is $\Delta y^+ = 15$ on either side of the splitter plate. However, the bottom and top walls of the experimental test section are only coarsely resolved using a spacing of $\Delta y^+ = 45$, since these regions are not of direct interest. The splitter plate (0.8 mm) is resolved using 7 equally spaced grid points to capture the initial vortex roll-up.

To resolve the sub-grid scalar field, 12 LEM cells are used in each LES cell in the region of interest. This resolution is determined as a compromise between computational efficiency and sub-grid scalar resolution needed to resolve the smallest scale of motion. The experiments[22] report that the average Bachelor scale for $M_c = 0.62$ is $\lambda_B \approx 0.8\mu m$. Here, $\lambda_B \approx 25\delta_w Re_w^{-3/4} Sc^{-1/2}$, where, δ_w is the vorticity thickness, Re_w is the Reynolds' number based on the vorticity thickness, and Sc is the Schmidt number. Based on this estimate, the LEM grid spacing resolves $5\lambda_B$ and $14\lambda_B$ on the supersonic and subsonic sides, respectively. This resolution is reasonable when compared to the experimental range.

Instantaneous flow visualization shows that the shear layer gets perturbed and rolls up into vortical structures; however this roll-up is considerably subdued compared to the roll-up observed in subsonic flows.[23,24] Figures 10(a) and (b) show respectively the contours of the filtered density and temperature at a representative instant. Formation of weak, oblique compression waves from the edge of the splitter plate is apparent in Fig. 10(a). Experiments[21] also reported the existence of similar waves from the edge of the

splitter plate due to the difficulty in exactly matching the pressures between the supersonic and the subsonic sides (a similar difficulty exists in the current study since all the details of the inflow are unavailable). Contours of density also reveal the delay in the formation of the large structures, and thus in the growth of the mixing layer. This is consistent with the observations made in the past.[1,2,25,21,26] It can be observed in the above figures that the mixing layer is pushed down toward the subsonic side within this test facility. This is consistent with the observation in the experiments[21] where a similar downward motion due to transverse pressure non-equilibrium was observed.

Details of the momentum mixing and other results have been reported elsewhere.[17,18,19] Here, we focus primarily on the scalar mixing results. In the experiments, the mean and the RMS of the mixture fraction were calculated using the probability density function (PDF) of the mixture fraction. In the current study, instantaneous data from within each LES cell is collected is collected over a long period and ensemble-averaged. Figures 11(a) and (b) show respectively, the profiles of the mean and the RMS fluctuations of the mixture fraction plotted in the similarity coordinate η. The mean and the RMS mixture fraction at different streamwise location shows that that these profiles collapses relatively well into a single profile, suggesting self-similarity. The mean profile shows a single inflection point for the LES-LEM case, consistent with experimental observation. However, the LES-GRAD-DIFF case shows multiple inflection points.

Figure 12 shows the PDF of the species mass fraction in at the transverse location corresponding to the similarity coordinate $\eta = 0$. The PDF peaks at $\xi \approx 0.4$ implying that the probable mixture fraction around the center of the mixing layer is 0.4. The overall agreement of LES-LEM with experiments[21] is again encouraging. Accurate prediction of the PDF of the mixture fraction implies that all the higher moments (e.g., mean and the RMS) can now be computed accurately. In contrast, LES-GRAD-DIFF predicts a much broader PDF with a lower peak indicating a diffusive nature of the solution. It is worth noting that in the LES-GRAD-DIFF model, the dynamic subgrid model for k^{sgs} is used to obtain ν_t and hence, the eddy diffusivity. Thus, the scalar profile is directly controlled by the eddy viscosity closure, whereas, in the LES-LEM closure, the momentum closure does not directly influence scalar diffusion and transport.

5.3.2 Comparison with Current Experiments

Simulations of cold flow in the wind tunnel without the step were conducted using a 205x150x15 grid and for the case with the step using a 235x139x15 grid. In both cases, the wall boundary layer is barely resolved and this is expected to be a problem for LES since the near-wall region is very critical. However, the initial effort was to do a "coarse" grid evaluation of the flow in the test facility. Figure 13 shows the stagnation temperature profile in the GT facility. It can be seen that although the wall is only slightly hot it does impact the prediction drastically. Both 2D and 3D results are shown in this figure. For this flow without any step, the 2D results are reasonable but it is noted that in general, LES requires full 3D simulation.

Figure 14 compares the predicted wall pressure in the tunnel with data. In our simulation, the inflow was adjusted to ensure there were no shocks or waves and the pressure is constant along the centerline, as expected. The experimental data shows some variation due to the presence of weak waves.

Finally, Figs. 15 and 16 compares the axial velocity and pitot pressure transverse profiles in the tunnel at various axial locations. The boundary grows very little in the tunnel and there is generally good agreement between the current simulation and data.

Some results for the rearward facing step flow also has been obtained. Figure 17 shows typical Mach number contours in the flow. The expansion fan at the step and the subsequent recompression near reattachment can be clearly seen. When compared to the experimental data, the reattachment distance is larger in the current simulation. It is not yet clear if this is a consequence of the inflow variations and the presence of weak waves seen in the experiments.

Figures 18 and 19 show the wall pressure variation and axial velocity profile downstream of the reattachment, respectively. In Fig. 18 there is reasonable agreement along the top wall but the pressure rise downstream of the reattachment on the bottom wall is predicted lower due to the over prediction of the reattachment length. This is also apparent in the velocity profile (Fig. 19).

It is noted that these results are preliminary since the experimental data is just now becoming available. Also, the PLIF data is still not available for scalar mixing which is the focus of this effort.

5.3.3 Supersonic Combustion Studies

Some studies have also been conducted for supersonic combustion. Both gaseous (Hydrogen) combustion[20] and liquid spray (heptane) combustion[27] using the current LES approach. For the hydrogen-air combustion case the experiments of Oevermann[28] were simulated and results compared for available data. For liquid spray case[27] experiments at WPAFB are simulated, however no direct comparison has been possible at this time. Some key highlights of the hydrogen case is reported here since the spray case is reported in a paper[27] in this conference.

The Oevermann test case is combustion in the base of a wedge-shaped injector shows schematically in Fig. 20. It consists of a series of injector holes in the spanwise direction and for the current simulation we have

simulated the central hole and the two-halves of the adjacent holes as shown in Fig. 21. In Fig. 21, Mach number isosurface is shown on top of a Z-vorticity plot. Periodic boundary in z direction is utilized.

A $250x121x25$ grid is used for the baseline calculations with grid clustered in the wake region and in the shear layer region to resolve the mixing. For LES-LEM, 12 LEM cells are used in the LES cells in the region downstream of the base of the wedge.

Density shadowgraph contour plot of the simulated flow-field is shown in Fig. 22 and compared to the experimental shadowgraph. It can be seen that the growth of the wake resulting from the volumetric expansion due to the reaction is not reproduced with great accuracy. However, the shock/shear layer interaction is well simulated. In particular, the impinging shock bends the shear layer, and the consequent flow direction matches the experimental behavior.

Experimental and computed mean temperature profiles at two different stations are shown in Fig. 23. As was expected, the infinite chemistry approach is not satisfactory. Scalar mixing does not occur, and the flame doesn't penetrate the wake behind the wedge. This results in a double-spike configuration, whose amplitudes are excessively large compared to experimental values. The EBU approach gives a better simulation of the heat release effect. It does not overshoot the experimental values, and in fact, tends to undershoot them. As a result of the poor scalar mixing even in this method, it can be seen that the two flame fronts issued from the wedge base corners do not collapse as the experiments describe. As a result, further downstream, a double reaction zone still appears in the LES-EBU case.

The subgrid LEM approach, on the other hand, shows an improved simulation of the heat release effect at both stations. The chemical species are efficiently mixed, and the flame fronts do penetrate the wake/shear layer created by the wedge, and collapse to form a single flame front, as observed in the experiments. The RANS simulation of Oevermann[28] did capture the collapse of the flame fronts, but overestimated the merging point, resulting in a wider hot zone, and a lower temperature. At the second station, both RANS and LEM approaches give a good estimate of the maximum temperature in the reacting region, but tend to spread the flame brush width. The oscillations observed in the temperature profiles in the LES-LEM might be due to a too short averaging time for this set of data. Extending this average would probably give more accurate results.

6 Concluding Remarks

In the present study, the progress in a combined experimental-numerical study on supersonic combustion is reported. In particular, the ability of a LES approach that incorporates subgrid mixing and combustion within the LES approach has been evaluated using available data. The advantage of LES-LEM is that it can account for scalar mixing and finite-rate kinetics without requiring closure. All these features are considered necessary for accurate prediction of scalar mixing and turbulent combustion. In general, it is shown that LES-LEM demonstrates good agreement with experimental data for supersonic spatial scalar mixing and also for gaseous combustion in the base of a wake of a flame holder, especially when compared to RANS and EBU approaches. Some preliminary comparison with flow in the GT facility is also shown, although further studies of scalar mixing is planned when data becomes available.

Acknowledgment

This work is supported by NASA University Institute at University of Florida under a grand NCC3-994.

References

[1] Papamoschou, D. and Roshko, A., "The compressible turbulent shear layer:an experimental study," *J. of Fluid Mech.*, Vol. 197, 1998, pp. 453–477.

[2] Elliott, G. S. and Samimy, M., "Compressibility effects in free shear layers," *Physics of Fluids*, Vol. 2, 1990, pp. 1231–1240.

[3] Kim, W.-W. and Menon, S., "A New Incompressible Solver for Large-Eddy Simulations," *International Journal of Numerical Fluid Mechanics*, Vol. 31, 1999, pp. 983–1017.

[4] Kim, W.-W. and Menon, S., "Numerical Modeling of Turbulent Premixed Flames in the Thin-Reaction-Zones Regime," *Combustion Science and Technology*, Vol. 160, 2000, pp. 119–150.

[5] Fureby, C., "Large-Eddy Simulation of Combustion Instabilities in a Jet Engine Afterburner Model," *Combustion Science and Technology*, Vol. 161, 2000, pp. 213–243.

[6] Chakravarthy, V. and Menon, S., "Large-Eddy Simulations of Turbulent Premixed Flames in the Flamelet Regime," *Combustion Science and Technology*, Vol. 162, 2001, pp. 175–222.

[7] Chakravarthy, V. and Menon, S., "Linear-Eddy Simulations of Reynolds and Schmidt Number Dependencies in Turbulent Scalar Mixing," *Physics of Fluids*, Vol. 13, 2001, pp. 488–499.

[8] Menon, S. and Calhoon, W., "Subgrid Mixing and Molecular Transport Modeling for Large-Eddy Simulations of Turbulent Reacting Flows," *Proc. of the Combustion Institute*, Vol. 26, 1996, pp. 59–66.

[9] Sankaran, V., Porumbel, I., and Menon, S., "Large-Eddy Simulation of a Single-Cup Gas-Turbine Combustor," *AIAA-2003-5083, 39th AIAA Joint Propulsion Conference*, 2003.

[10] Shani, S., Tran, T., Genin, F., Menon, S., and Seitzman, J., "Characterization of Liquid Fuel Mixing ina Scramjet Flowfield," *AIAA-03-6990*, 2003.

[11] Segal, C. and Young, C. D., "Development of an Experimentally-Flexible Facility for Mixing-Combustion Interactions in Supersonic Flow," *Journal of Energy Resource Technology*, Vol. 118, 1996, pp. 152–158.

[12] Kim, W.-W., Menon, S., and Mongia, H. C., "Large Eddy Simulations of a Gas Turbine Combustor Flow," *Combustion Science and Technology*, Vol. 143, 1999, pp. 25–62.

[13] Menon, S., Yeung, P.-K., and Kim, W.-W., "Effect of Subgrid Models on the Computed Interscale Energy Transfer in Isotropic Turbulence," *Computers and Fluids*, Vol. 25, No. 2, 1996, pp. 165–180.

[14] Chakravarthy, V. and Menon, S., "Large-Eddy Simulations of Turbulent Premixed Flames in the Flamelet Regime," *Combustion Science and Technology*, Vol. 162, 2001, pp. 175–222.

[15] Kerstein, A. R., "Linear-Eddy Model of Turbulent Transport II," *Combustion and Flame*, Vol. 75, 1989, pp. 397–413.

[16] Pope, S. B., "Turbulent Flame propagation in partially premixed flames," *Proceedings of the Summer Program, Center for Turbulence Research*, 1996.

[17] Sankaran, V. and Menon, S., "LES of Scalar Mixing in Supersonic Shear Layers," *Proc. of the Combustion Institute*, Vol. 30, 2004.

[18] Sankaran, V. and Menon, S., "Subgrid Scalar Model for Supersonic Mixing," *Proc. of the 10th European Turbulence Conference*, 2004.

[19] Sankaran, V. and Menon, S., "A Subgrid Mixing Model for LES of Supersonic Combustion," *AIAA-2004-0801*, 2004.

[20] Genin, F., Chernyavsky, B., and Menon, S., "Large Eddy Simulation of Scramjet Combustion Using a Subgrid Mixing Model," *AIAA 2003-7035*, 2003.

[21] Clemens, N. T. and Mungal, M. G., "Large-scale-structure and entrainment in the supersonic mixing layer," *J. of Fluid Mech.*, Vol. 284, 1995, pp. 171–216.

[22] Island, T. C., *Quantitative scalar measurements and mixing enhancement in compressible shear layers*, Ph.D. thesis, Stanford University, Mechanical Engineering Department, CA, April 1997.

[23] Brown, G. L. and Roshko, A., "On Density effects and Large Structures in Turbulent Mixing Layers," *J. of Fluid Mech.*, Vol. 84, 1974, pp. 775–816.

[24] Ho, C. M. and Huerre, P., "Perturbed free shear layers," *Annual Review of Fluid Mechanics*, Vol. 16, 1984, pp. 365–424.

[25] Goebel, S. G. and Dutton, J. C., "Experimental study of compressible turbulent mixing layers," *AIAA Journal*, Vol. 29, 1991, pp. 538–546.

[26] Sandham, N. D. and Reynolds, W. C., "Three dimensional simulations of large eddies in the compressible mixing layer," *Journal of Fluid Mechanics*, Vol. 224, 1991, pp. 133–158.

[27] Genin, F. and Menon, S., "LES of Supersonic Combustion of Hydrocarbon Spray in a SCRAMJET," *AIAA 2004-4132*, 2003.

[28] Oevermann, M., "Numerical Investigation of Turbulent Combustion in a SCRAMJET Using Flamelet Modeling," *Aerospace Science and Technology*, Vol. 4, 2000, pp. 463–480.

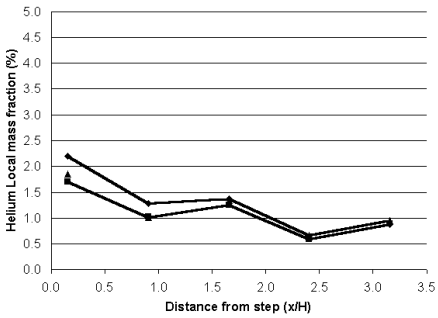

a) Helium Profiles for $P_{0He} = 5.4$ atm

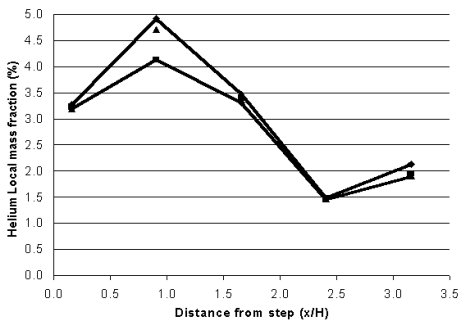

b) Helium Profiles for $P_{0He} = 12$ atm

Fig. 8 Axial Helium mass fraction profiles

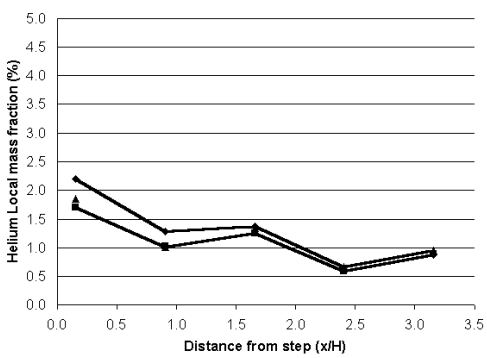

a) Helium Profiles for $P_{0He} = 5.4$ atm

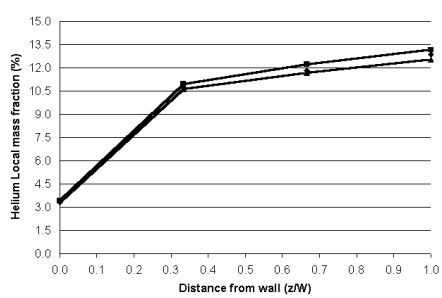

b) Helium Profiles for $P_{0He} = 12$ atm

Fig. 9 Transverse Helium mass fraction profiles at $x/H = 1.7$.

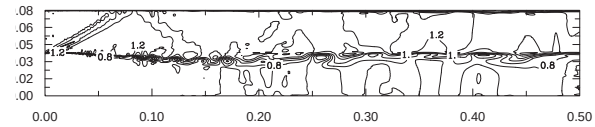

a) Density

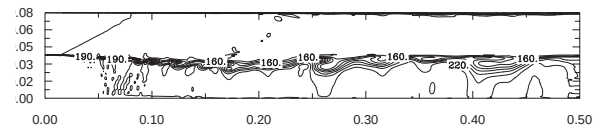

b) Temperature

Fig. 10 Contours of the filtered density and temperature in the shear layer. Density contours range from 0 to 2 Kg/m^3 with an interval of 0.2 Kg/m^3. Contours of temperature range from 131 K to 273 K with an interval of 10 K.

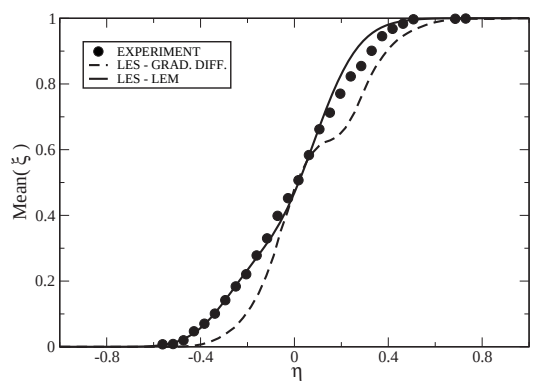

a) Mean Mixture Fraction

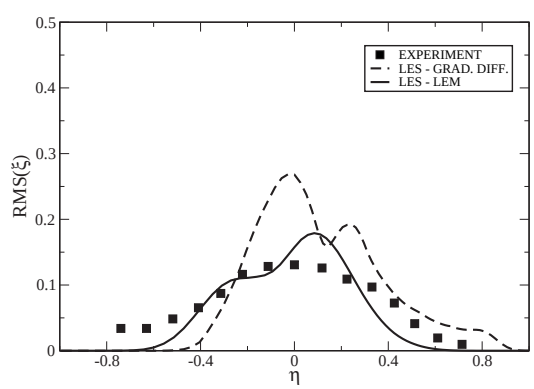

b) RMS Mixture Fraction

Fig. 11 Transverse profiles of mean and RMS mixture fraction.

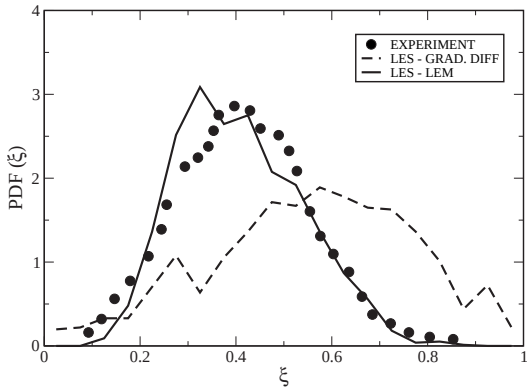

Fig. 12 PDF of the mixture fraction in the supersonic stream at $\eta = 0$.

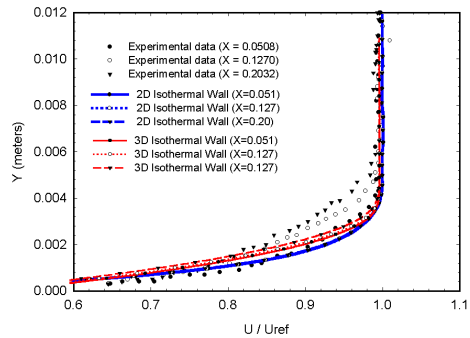

Fig. 15 Axial velocity profiles in the GT tunnel

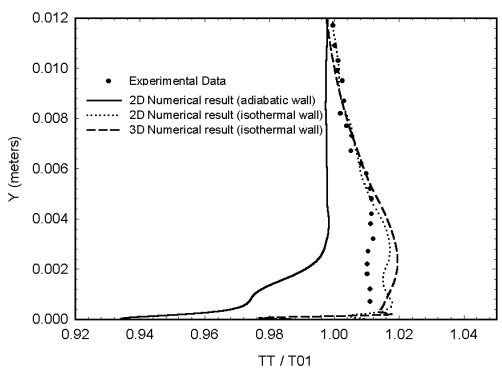

Fig. 13 Stagnation temperature profile in the GT tunnel

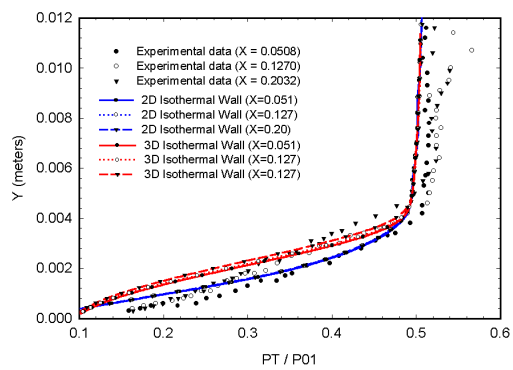

Fig. 16 Pitot pressure profiles in the GT tunnel

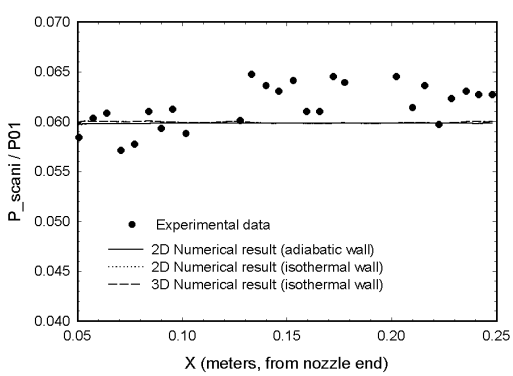

Fig. 14 Wall pressure in the GT tunnel

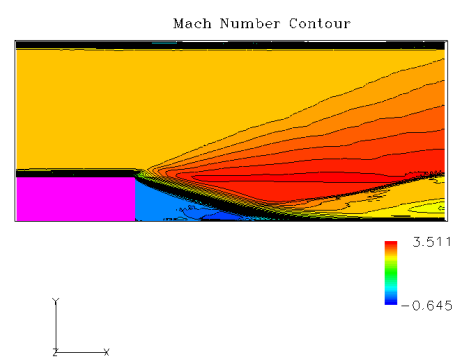

Fig. 17 Mach contours with the step

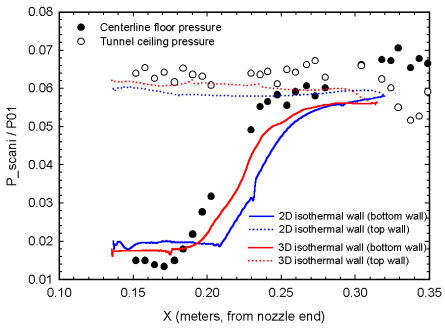

Fig. 18 Wall pressure with the step

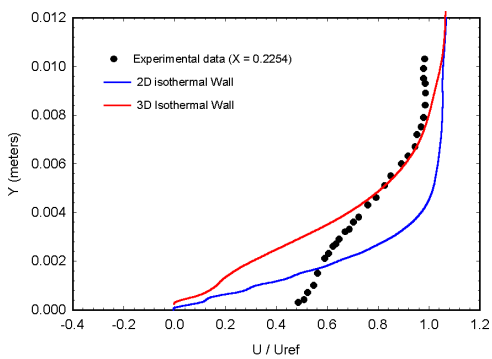

Fig. 19 Velocity profile downstream of reattachment

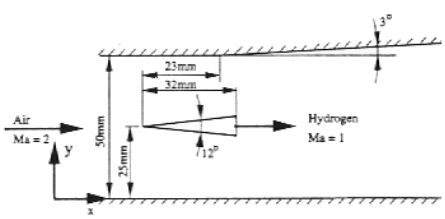

Fig. 20 Experimental Configuration[28]

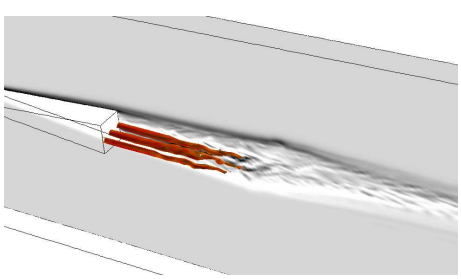

Fig. 21 Hydrogen injection holes / Vorticity for the burning case.

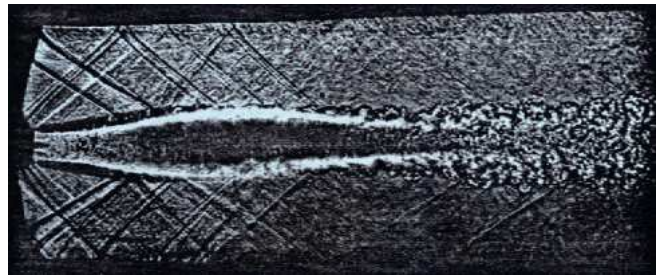

a) Experimental

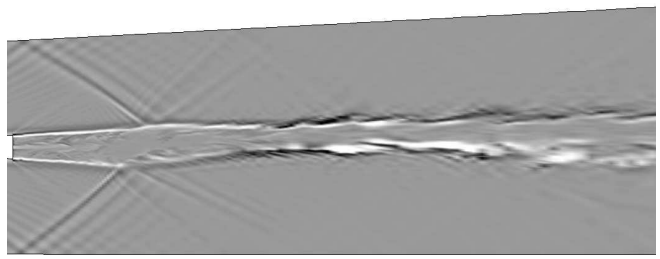

b) $\nabla^2\rho$ field

Fig. 22 Instantaneous shadowgraphs

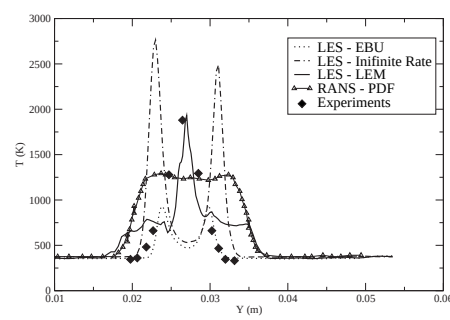

a) x = 58 mm from the base of the wedge

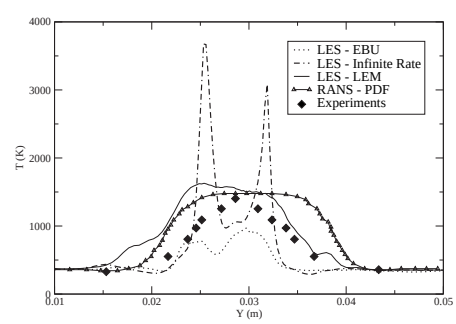

b) x = 156 mm from the base of the wedge

Fig. 23 Temperature profiles at two axial stations for the reacting LES.